Temporal Homogenization Modeling of Viscoelastic Asphalt Concretes and Pavement Structures under Large Numbers of Load Cycles

Hanyu Zhang, S.M.ASCE,[1] **Gordon Airey**, Ph.D.,[2] **Yuqing Zhang**, Ph.D.[3]

[1]Ph.D. Candidate, Nottingham Transportation Engineering Centre (NTEC), Faculty of Engineering, University of Nottingham, University Park, Nottingham, NG7 2RD, United Kingdom; email: hanyu.zhang@nottingham.ac.uk

[2]Professor, Nottingham Transportation Engineering Centre (NTEC), Faculty of Engineering, University of Nottingham, University Park, Nottingham, NG7 2RD, United Kingdom; email: gordon.airey@nottingham.ac.uk

[3]Professor, School of Transportation, Southeast University, 2 Southeast University Road, Nanjing, 211189, China; email: zhangyuqing@seu.edu.cn **(Corresponding Author)**

ABSTRACT

This paper aims to introduce a highly efficient computational model compared to the current cycle-by-cycle simulation strategy to compute the viscoelastic responses of asphalt concretes and pavement structures under large numbers of cyclic loading. An explicit constitutive relation for viscoelastic solids in multiple time scales was developed based on the temporal homogenization. The original initial-boundary value problem was divided into a global part in the slow time scale and a local part in the fast time scale. Two simulation studies were presented to validate the computational accuracy and efficiency of the proposed model: (a) a cylindrical asphalt concrete subject to a uniaxial cyclic compression load; and (b) a pavement structure subject to a locally cyclic loading. The laboratory test results and field measurements were compared with the modeled responses to validate the models before comparing with the reference solutions. Results indicate that the temporal homogenization-based viscoelastic model saves considerable computational cost and maintains a satisfactory accuracy. The absolute values of relative error of the modeled responses between the time homogenization and reference solutions are lower than 1% and 4% for the cylindrical asphalt concrete and pavement structure under locally cyclic loadings, respectively. Based on the proposed computational approach, only 4 minutes are needed to model the response of a cylindrical asphalt concrete subject to 10^4 repeated load cycles under a uniaxial compression load. The computational time is reduced from 7 hours of the reference solution to 38 minutes of the temporal homogenization solution to model 10^3 load cycles of a viscoelastic pavement structure.

AUTHOR KEYWORDS: Temporal Homogenization; Asymptotic Analysis; Viscoelasticity; Cyclic Loading; Asphalt Concrete; Asphalt Pavement

INTRODUCTION

Accurately predicting the long-term performance and obtaining the essential design criteria (e.g., rut depth and percent of the crack area) of asphalt pavements is one of the most significant challenges in pavement engineering. In the past decades, considerable regressions and field calibrations were employed to develop the empirical functions which transfer the mechanical responses at specific pavement positions (e.g., the bottom of asphalt layer) to the long-term performance indices of asphalt pavements (Abdelfattah et al. 2021; Tarefder and Rodriguez-Ruiz 2013). The approach above consists of the long-term performance prediction of the mainstream pavement design method known as the Mechanistic-Empirical Pavement Design Guide (MEPDG) (AASHTO 2020). In MEPDG, each pavement distress prediction model requires inputting the responses calculated by the structural response model which is a multilayer elastic program (Kim et al. 2007). As can be seen, the main drawbacks of the structural response model are: (a) unrealistic to describe the complex mechanical behaviors (viscoelasticity, viscoplasticity, and continuum damage) of asphalt concretes; and (b) unable to provide the accurate stress state at each load cycle.

The current pavement performance models in MEPDG were proposed 30 years ago; thus, the main obstacles for developing a pure mechanistic design method at that time were the lack of advanced computing platforms and efficient computational approaches (Lytton et al. 1993). From the perspective of constitutive modeling of asphalt pavements, the asphalt concrete is regarded as a viscoelastic material and its constitutive relation is usually described via the convolutional integrations (Kim 2009). Time integration algorithms are needed when one is trying to model the mechanical responses of asphalt pavements using finite element (FE) modeling. In this case, obtaining the pavement long-term (e.g., 20 years) responses is impossible based on the conventional time-domain computation, as the time steps in FE modeling are of the order of seconds. From the perspective of initial-boundary value problems (IBVPs) for asphalt pavements, the vehicle load is usually simplified as a cyclic loading input with a haversine waveform, which means the time steps in the FE modeling need to be small enough to capture the rapid variations of mechanical responses within each load cycle. Over millions of load cycles need to be modeled to obtain the long-term performance of asphalt pavements; thus, the required computational resources are almost unaffordable even for a high-performance computing platform.

An ideal approach for predicting the long-term pavement performance is to conduct the cycle-by-cycle modeling of pavement responses, as the permanent deformation and structural damage are intimately associated with the stress state at each load cycle. Different methods have been utilized to improve the modeling efficiency of pavement responses, including using a 2D plane strain model or a semi-analytical FE modeling (Chen et al. 2017; Shen et al. 2022). However, it is still unknown if the methods above can provide the pavement responses under a large number of load cycles within an acceptable computing time. Another method for pavement long-term performance prediction was developed by the North Carolina State University (NCSU) (Eslaminia et al. 2012; Eslaminia and Guddati 2016). Compared to the MEPDG, this method uses a layered viscoelastic continuum damage (LVECD) program for calculating the pavement responses and damage conditions, while still requiring an extrapolation scheme so that the millions of load cycles can be reduced to the hundred independent analyses.

The above approaches are usually used in the asphalt pavement engineering for the long-term pavement performance prediction. However, modeling the mechanical responses of solids under large numbers of cyclic loading is widely needed in the field of solid mechanics (Lemaitre and Desmorat 2005). Many methods have been proposed for handling the long-term mechanical response modeling of different materials with varying constitutive relations (e.g., cement concretes, polymers, metals, and biomaterials), including the large time increments (LATIN) method, cycle jump, and temporal homogenization (Cognard and Ladevèze 1993; Cojocaru and Karlsson 2006; Devulder et al. 2010). The key concept of the above computational methods is to apply a large time increment and separate the IBVP into a global and a local one via numerical approximations. The idea seems intuitive as modeling the mechanical response evolution of solids under large numbers of cyclic loading is indeed a multiscale problem in the time domain, as it involves the slow evolution in the long term and the fast variations in the short term. The temporal homogenization method inserts the numerical approximation formula into the material constitutive relations, while the other two methods require an external extrapolation algorithm and the balance between the computational efficiency and accuracy highly depends on the user-defined extrapolation scheme. Thus, this paper selects the temporal homogenization method to model the long-term mechanical responses of asphalt pavements, although all three methods have good computational gain. This paper is one of the few attempts in the pavement engineering field to apply the temporal homogenization method for modeling the pavement long-term mechanical responses with a focus on the viscoelastic modeling (Behnke et al. 2019; Behnke and Kaliske 2018). By successfully implementing a mechanistic framework for the long-term pavement performance prediction, the pavement design can more rely on the material inherent properties instead of using redundant empirical transfer functions.

In summary, this paper focuses on introducing a highly efficient computational model based on the temporal homogenization to predict the long-term mechanical responses of the viscoelastic asphalt concretes and pavement structures. This paper is organized as follows. The next section details the fundamentals and formula of the temporal homogenization method and its implementation in the constitutive relations of viscoelastic solids (asphalt concrete is taken as a verification example). The following section presents the modeling scenarios including a cylindrical asphalt concrete sample and a pavement structure and shows the validation results of the temporal homogenization and reference solutions. Conclusions and recommendations are summarized in the last section.

METHODOLOGIES

Fundamentals of Temporal Homogenization Method

The temporal homogenization method was proposed based on the asymptotic analysis/series, a mathematical approximation for describing limiting behaviors. It is a direct extension of the spatial homogenization which definition is shown as follows. If the period of the structure is small compared to the size of the region in which the system is to be studied, then an asymptotic analysis is called for: to obtain an asymptotic expansion of the solution in terms of a small parameter ς which is the ratio of the period of the structure to a typical length in the region. In other words, to obtain by systematic expansion procedures the passage from a microscopic description to a macroscopic description of the behavior of the system (Bensoussan et al. 1978; Guennouni 1988; Yu and Fish 2002a). To solve the above problems, using the multiple (time or space) scales to construct the asymptotic expansion is one of the solutions.

Based on the descriptions above, the temporal homogenization method is used to address the IBVPs with rapidly varying periodic loading via two time scales. One is measuring the evolutions within the entire loading time (in the slow time scale), and the other is measuring the variations within one load cycle (in the fast time scale). The following content details the concepts and formula of temporal homogenization.

First of all, two time scales and a scaling parameter are introduced as shown in **Figure 1**, which has been proposed in the literature (Yu and Fish 2002a). For the viscoelastic materials under periodically cyclic loading, an intrinsic time t_r is related to its relaxation time; it serves as the characteristic length of the slow time scale t and describes a relatively long-term behavior compared to a single period of loading. **Equation 1** shows the definition of t_r (Yu and Fish 2002b). The period of external loading denoted by τ_0 serves as the characteristic time length of the fast time scale τ, describing the rapidly varying behavior within each load cycle. To characterize the fast-varying features of response fields (stress, strain, and displacement) induced by the locally periodic loading, a small positive scaling parameter ς is defined in **Equation 2** so that the fast time scale τ can be defined via **Equation 3**. With the τ-periodicity assumption, all the response fields ϕ can be described using **Equation 4**. The first-order time differentiation of the response fields can be written as **Equation 5** according to the chain rule.

$$t_r = O\{\|\boldsymbol{V_{ijkl}}\|/\|\boldsymbol{L_{ijkl}}\|\} \tag{1}$$

where t_r is the material intrinsic time that accounts for the slow time scale; $\|*\|$ is the norm of $*$; $\boldsymbol{V_{ijkl}}$ is the component of viscosity tensor; and $\boldsymbol{L_{ijkl}}$ is the component of elastic stiffness tensor.

$$\varsigma = \tau_0/t_r\,,\ \varsigma \ll 1 \tag{2}$$

where ς is the scaling parameter for differentiating the two time scales; τ_0 and t_r are the characteristic lengths of the fast time scale and slow time scale.

$$\tau = t/\varsigma \tag{3}$$

where τ is the fast time scale and t is the slow time scale.

$$\phi^{\varsigma}(\vec{\boldsymbol{x}}, T) = \phi(\vec{\boldsymbol{x}}, t, \tau) = \phi(\vec{\boldsymbol{x}}, t, \tau + k\tau_0), k \in \mathbb{Z} \tag{4}$$

where $\vec{\boldsymbol{x}}$ denotes the position vector in space; T is the observation time in the natural time scale: $T = T(t, \tau)$; ϕ^{ς} is the response field in the natural time scale; and ϕ is the response field in the combination of slow time scale and fast time scale.

$$\dot{\phi}^{\varsigma} = \phi_{,t} + \varsigma^{-1}\phi_{,\tau} \tag{5}$$

where $\dot{\phi}^{\varsigma} = \frac{d\phi^{\varsigma}}{dT}$; $\phi_{,t} = \frac{\partial\phi}{\partial t}$; and $\phi_{,\tau} = \frac{\partial\phi}{\partial\tau}$.

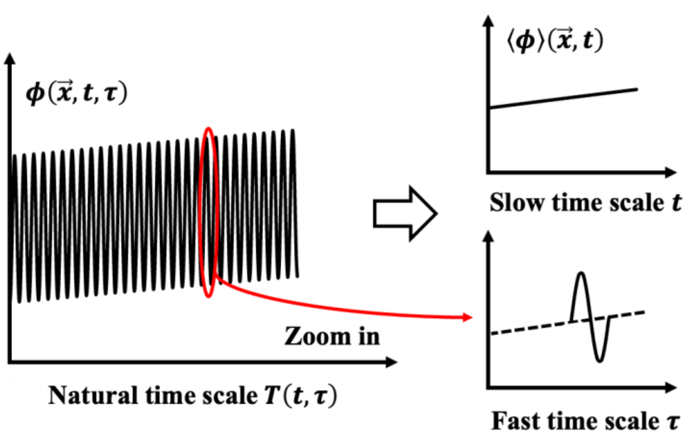

Figure 1. Illustration of two time scales.

Secondly, another important concept of temporal homogenization is to use asymptotic expansion to represent each response field and achieve the decompositions of initial response fields which are in the natural time scale T. Supposing that every response field is periodic and the scaling parameter is small enough, ϕ^{ς} can be expanded into an asymptotic series of powers of ς, as shown in **Equation 6** (Haouala and Doghri 2015).

$$\phi^{\varsigma} = \sum_{n=0}^{\infty} \varsigma^n \phi^n(\vec{x}, t, \tau) \tag{6}$$

where ϕ^n are τ-periodic functions; for the ϕ^n, n denotes the order of terms in the expansion; for the ς^n, n denotes the power. This asymptotic expansion of the response fields can be regarded as consisting of a leading term $\phi^0(\vec{x}, t, \tau)$, plus a series of terms with rapidly decreasing amplitude (Haouala and Doghri 2015).

Thirdly, to decompose the initial response fields into a global (in the slow time scale) and a local (in the fast time scale) part, a temporal averaging operator $\langle \bullet \rangle$ on the τ-periodic response fields is introduced in **Equation 7**. As can be seen, all the response fields only depend on the slow time scale after conducting the temporal averaging transformation.

$$\langle \phi \rangle(\vec{\boldsymbol{x}}, t) = \frac{1}{\tau_0} \int_{\tau}^{\tau+\tau_0} \phi(\vec{\boldsymbol{x}}, t, \tau)\, d\tau \tag{7}$$

Thus, the following decompositions for each response field can be obtained:

$$\boldsymbol{\sigma}_{ij}^{\boldsymbol{m}}(\vec{\boldsymbol{x}}, t, \tau) = \langle \boldsymbol{\sigma}_{ij}^{\boldsymbol{m}} \rangle(\vec{\boldsymbol{x}}, t) + \boldsymbol{\Phi}_{ij}^{\boldsymbol{m}}(\vec{\boldsymbol{x}}, t, \tau) \tag{8}$$

$$\boldsymbol{\varepsilon}_{ij}^{\boldsymbol{m}}(\vec{\boldsymbol{x}}, t, \tau) = \langle \boldsymbol{\varepsilon}_{ij}^{\boldsymbol{m}} \rangle(\vec{\boldsymbol{x}}, t) + \boldsymbol{\Psi}_{ij}^{\boldsymbol{m}}(\vec{\boldsymbol{x}}, t, \tau) \tag{9}$$

$$\boldsymbol{u}_{i}^{\boldsymbol{m}}(\vec{\boldsymbol{x}}, t, \tau) = \langle \boldsymbol{u}_{i}^{\boldsymbol{m}} \rangle(\vec{\boldsymbol{x}}, t) + \boldsymbol{\chi}_{i}^{\boldsymbol{m}}(\vec{\boldsymbol{x}}, t, \tau) \tag{10}$$

where $\boldsymbol{\sigma}_{ij}^{\boldsymbol{m}}(\vec{\boldsymbol{x}}, t, \tau)$, $\boldsymbol{\varepsilon}_{ij}^{\boldsymbol{m}}(\vec{\boldsymbol{x}}, t, \tau)$, and $\boldsymbol{u}_{i}^{\boldsymbol{m}}(\vec{\boldsymbol{x}}, t, \tau)$ are the stress, strain, and displacement fields for the original IBVP, respectively; $\langle \boldsymbol{\sigma}_{ij}^{\boldsymbol{m}} \rangle(\vec{\boldsymbol{x}}, t)$, $\langle \boldsymbol{\varepsilon}_{ij}^{\boldsymbol{m}} \rangle(\vec{\boldsymbol{x}}, t)$, and $\langle \boldsymbol{u}_{i}^{\boldsymbol{m}} \rangle(\vec{\boldsymbol{x}}, t)$ are the global part of the stress, strain, and displacement fields in the slow time scale; $\boldsymbol{\Phi}_{ij}^{\boldsymbol{m}}(\vec{\boldsymbol{x}},t,\tau)$, $\boldsymbol{\Psi}_{ij}^{\boldsymbol{m}}(\vec{\boldsymbol{x}},t,\tau)$, and $\boldsymbol{\chi}_{i}^{\boldsymbol{m}}(\vec{\boldsymbol{x}},t,\tau)$ are the local part of the stress, strain, and displacement fields in the fast time scale.

Temporal Homogenization Formula for Asphalt Concretes

In this paper, an explicit constitutive relation of a solid-like generalized Maxwell model is used for describing the linear viscoelasticity of asphalt concretes, as shown in **Equations 11** and **12** (Zhang and Zhang 2023). The explicit constitutive equation is clearer and easier to use in writing the weak formula and time discretization in FE modeling.

$$\boldsymbol{\sigma}_{ij}^{\varsigma} = K_\infty \boldsymbol{\varepsilon}_{kk}^{\varsigma,ve}\boldsymbol{\delta}_{ij} + 2G_\infty \boldsymbol{e}_{ij}^{\varsigma,ve} + \sum_{m=1}^{M}\left[K_m\left(\boldsymbol{\varepsilon}_{kk}^{\varsigma,ve}-\boldsymbol{\varepsilon}_{kk}^{\varsigma,m\cdot vi}\right)\boldsymbol{\delta}_{ij} + 2G_m\left(\boldsymbol{e}_{ij}^{\varsigma,ve}-\boldsymbol{e}_{ij}^{\varsigma,m\cdot vi}\right)\right] \qquad (11)$$

$$\begin{cases} a_T\tau_m\dot{\boldsymbol{\varepsilon}}_{kk}^{\varsigma,m\cdot vi} + \boldsymbol{\varepsilon}_{kk}^{\varsigma,m\cdot vi} - \boldsymbol{\varepsilon}_{kk}^{\varsigma,ve} = 0 \\ a_T\tau_m\dot{\boldsymbol{e}}_{ij}^{\varsigma,m\cdot vi} + \boldsymbol{e}_{ij}^{\varsigma,m\cdot vi} - \boldsymbol{e}_{ij}^{\varsigma,ve} = 0 \end{cases} \qquad (12)$$

where $\boldsymbol{\sigma}_{ij}^{\varsigma}$ is the stress tensor; $\boldsymbol{\varepsilon}_{kk}^{\varsigma,ve}$ and $\boldsymbol{e}_{ij}^{\varsigma,ve}$ are the viscoelastic volumetric and deviatoric strains, respectively; $\boldsymbol{\varepsilon}_{kk}^{\varsigma,m\cdot vi}$ and $\boldsymbol{e}_{ij}^{\varsigma,m\cdot vi}$ are the viscous volumetric and deviatoric strains resulted from the m^{th} dashpot (m=1, 2, …, M) in the generalized Maxwell model; K_∞ and G_∞ are the long-term equilibrium bulk and shear moduli; K_m and G_m are the components of the relaxation bulk and shear moduli; τ_m are the components of relaxation time; $\boldsymbol{\delta}_{ij}$ is the Kronecker delta; and a_T is the time-temperature shift factor.

The asymptotically expanded formula of **Equations 11** and **12** can be written as follows based on **Equation 6**.

$$\sum_{n=0}^{\infty}\varsigma^n\,\boldsymbol{\sigma}_{ij}^{\boldsymbol{n}} = K_\infty\sum_{n=0}^{\infty}\varsigma^n\,\boldsymbol{\varepsilon}_{kk}^{\boldsymbol{n},\boldsymbol{ve}}\boldsymbol{\delta}_{ij} + 2G_\infty\sum_{n=0}^{\infty}\varsigma^n\,\boldsymbol{e}_{ij}^{\boldsymbol{n},\boldsymbol{ve}} + \sum_{m=1}^{M}\Big[K_m\Big(\sum_{n=0}^{\infty}\varsigma^n\,\boldsymbol{\varepsilon}_{kk}^{\boldsymbol{n},\boldsymbol{ve}} - \sum_{n=0}^{\infty}\varsigma^n\,\boldsymbol{\varepsilon}_{kk}^{\boldsymbol{n},\boldsymbol{m}\cdot\boldsymbol{vi}}\Big)\boldsymbol{\delta}_{ij} + 2G_m\Big(\sum_{n=0}^{\infty}\varsigma^n\,\boldsymbol{e}_{ij}^{\boldsymbol{n},\boldsymbol{ve}} - \sum_{\boldsymbol{n}=\boldsymbol{0}}^{\infty}\boldsymbol{\varsigma}^{\boldsymbol{n}}\,\boldsymbol{e}_{ij}^{\boldsymbol{n},\boldsymbol{m}\cdot\boldsymbol{vi}}\Big)\Big] \qquad (13)$$

$$\begin{cases} a_T\tau_m\sum_{n=0}^{\infty}\varsigma^n\,\dot{\boldsymbol{\varepsilon}}_{kk}^{\boldsymbol{n},\boldsymbol{m}\cdot\boldsymbol{vi}} + \sum_{n=0}^{\infty}\varsigma^n\,\boldsymbol{\varepsilon}_{kk}^{\boldsymbol{n},\boldsymbol{m}\cdot\boldsymbol{vi}} - \sum_{n=0}^{\infty}\varsigma^n\,\boldsymbol{\varepsilon}_{kk}^{\boldsymbol{n},\boldsymbol{ve}} = 0 \\ a_T\tau_m\sum_{n=0}^{\infty}\varsigma^n\,\dot{\boldsymbol{e}}_{ij}^{\boldsymbol{n},\boldsymbol{m}\cdot\boldsymbol{vi}} + \sum_{n=0}^{\infty}\varsigma^n\,\boldsymbol{e}_{ij}^{\boldsymbol{n},\boldsymbol{m}\cdot\boldsymbol{vi}} - \sum_{n=0}^{\infty}\varsigma^n\,\boldsymbol{e}_{ij}^{\boldsymbol{n},\boldsymbol{ve}} = 0 \end{cases} \qquad (14)$$

Here the idea is to equate the terms having the same power of ς of **Equations 13** and **14** to obtain the different order of problems (Bhattacharyya et al. 2020).

-1 order problem:

Equate the terms having ς^{-1} in **Equations 13** and **14**, then it yields:

$$\begin{cases} {\boldsymbol{\varepsilon}_{\boldsymbol{kk}}^{\mathbf{0},\boldsymbol{m}\cdot\boldsymbol{vi}}}_{,\tau} = 0 \\ {\boldsymbol{e}_{\boldsymbol{ij}}^{\mathbf{0},\boldsymbol{m}\cdot\boldsymbol{vi}}}_{,\tau} = 0 \end{cases} \tag{15}$$

Equation 15 means the zero-order terms of viscous volumetric and deviatoric strains for each Maxwell brunch, $\boldsymbol{\varepsilon}_{\boldsymbol{kk}}^{\mathbf{0},\boldsymbol{m}\cdot\boldsymbol{vi}}$ and $\boldsymbol{e}_{\boldsymbol{ij}}^{\mathbf{0},\boldsymbol{m}\cdot\boldsymbol{vi}}$, only depend on the slow time scale. Based on this finding and the **Equations 7** and **9**, the following relations can be concluded:

$$\begin{cases} \boldsymbol{\varepsilon}_{\boldsymbol{kk}}^{\mathbf{0},\boldsymbol{m}\cdot\boldsymbol{vi}} = \langle \boldsymbol{\varepsilon}_{\boldsymbol{kk}}^{\mathbf{0},\boldsymbol{m}\cdot\boldsymbol{vi}} \rangle \\ \boldsymbol{e}_{\boldsymbol{ij}}^{\mathbf{0},\boldsymbol{m}\cdot\boldsymbol{vi}} = \langle \boldsymbol{e}_{\boldsymbol{ij}}^{\mathbf{0},\boldsymbol{m}\cdot\boldsymbol{vi}} \rangle \end{cases} \tag{16}$$

0 order problem:

Equate the terms without ς in **Equations 13** and **14**, then it yields:

$$\boldsymbol{\sigma}_{\boldsymbol{ij}}^{\mathbf{0}} = K_\infty \boldsymbol{\varepsilon}_{\boldsymbol{kk}}^{\mathbf{0},\boldsymbol{ve}} \boldsymbol{\delta}_{\boldsymbol{ij}} + 2G_\infty \boldsymbol{e}_{\boldsymbol{ij}}^{\mathbf{0},\boldsymbol{ve}} + \sum_{m=1}^{M} \left[K_m \left(\boldsymbol{\varepsilon}_{\boldsymbol{kk}}^{\mathbf{0},\boldsymbol{ve}} - \boldsymbol{\varepsilon}_{\boldsymbol{kk}}^{\mathbf{0},\boldsymbol{m}\cdot\boldsymbol{vi}} \right) \boldsymbol{\delta}_{\boldsymbol{ij}} + 2G_m \left(\boldsymbol{e}_{\boldsymbol{ij}}^{\mathbf{0},\boldsymbol{ve}} - \boldsymbol{e}_{\boldsymbol{ij}}^{\mathbf{0},\boldsymbol{m}\cdot\boldsymbol{vi}} \right) \right] \tag{17}$$

$$\begin{cases} a_T \tau_m \left({\boldsymbol{\varepsilon}_{\boldsymbol{kk}}^{\mathbf{0},\boldsymbol{m}\cdot\boldsymbol{vi}}}_{,t} + {\boldsymbol{\varepsilon}_{\boldsymbol{kk}}^{\mathbf{1},\boldsymbol{m}\cdot\boldsymbol{vi}}}_{,\tau} \right) + \boldsymbol{\varepsilon}_{\boldsymbol{kk}}^{\mathbf{0},\boldsymbol{m}\cdot\boldsymbol{vi}} - \boldsymbol{\varepsilon}_{\boldsymbol{kk}}^{\mathbf{0},\boldsymbol{ve}} = 0 \\ a_T \tau_m \left({\mathbf{e}_{\boldsymbol{ij}}^{\mathbf{0},\boldsymbol{m}\cdot\boldsymbol{vi}}}_{,t} + {\mathbf{e}_{\boldsymbol{ij}}^{\mathbf{1},\boldsymbol{m}\cdot\boldsymbol{vi}}}_{,\tau} \right) + \boldsymbol{e}_{\boldsymbol{ij}}^{\mathbf{0},\boldsymbol{m}\cdot\boldsymbol{vi}} - \boldsymbol{e}_{\boldsymbol{ij}}^{\mathbf{0},\boldsymbol{ve}} = 0 \end{cases} \tag{18}$$

The zero-order constitutive relation in the slow time scale is shown as follows by applying the averaging operator defined in **Equation 7**.

$$\langle \boldsymbol{\sigma}_{\boldsymbol{ij}}^{\mathbf{0}} \rangle = K_\infty \langle \boldsymbol{\varepsilon}_{\boldsymbol{kk}}^{\mathbf{0},\boldsymbol{ve}} \rangle \boldsymbol{\delta}_{\boldsymbol{ij}} + 2G_\infty \langle \boldsymbol{e}_{\boldsymbol{ij}}^{\mathbf{0},\boldsymbol{ve}} \rangle + \sum_{m=1}^{M} \left[K_m \left(\langle \boldsymbol{\varepsilon}_{\boldsymbol{kk}}^{\mathbf{0},\boldsymbol{ve}} \rangle - \langle \boldsymbol{\varepsilon}_{\boldsymbol{kk}}^{\mathbf{0},\boldsymbol{m}\cdot\boldsymbol{vi}} \rangle \right) \boldsymbol{\delta}_{\boldsymbol{ij}} + 2G_m \left(\langle \boldsymbol{e}_{\boldsymbol{ij}}^{\mathbf{0},\boldsymbol{ve}} \rangle - \langle \boldsymbol{e}_{\boldsymbol{ij}}^{\mathbf{0},\boldsymbol{m}\cdot\boldsymbol{vi}} \rangle \right) \right] \tag{19}$$

$$\begin{cases} a_T \tau_m \langle \boldsymbol{\varepsilon}_{\boldsymbol{kk}}^{\mathbf{0},\boldsymbol{m}\cdot\boldsymbol{vi}} \rangle_{,t} + \langle \boldsymbol{\varepsilon}_{\boldsymbol{kk}}^{\mathbf{0},\boldsymbol{m}\cdot\boldsymbol{vi}} \rangle - \langle \boldsymbol{\varepsilon}_{\boldsymbol{kk}}^{\mathbf{0},\boldsymbol{ve}} \rangle = 0 \\ a_T \tau_m \langle \boldsymbol{e}_{\boldsymbol{ij}}^{\mathbf{0},\boldsymbol{m}\cdot\boldsymbol{vi}} \rangle_{,t} + \langle \boldsymbol{e}_{\boldsymbol{ij}}^{\mathbf{0},\boldsymbol{m}\cdot\boldsymbol{vi}} \rangle - \langle \boldsymbol{e}_{\boldsymbol{ij}}^{\mathbf{0},\boldsymbol{ve}} \rangle = 0 \end{cases} \tag{20}$$

The zero-order constitutive relation in the fast time scale is shown as follows based on **Equations 8**, **9**, and **16** to **20**.

$$\boldsymbol{\Phi}_{\boldsymbol{ij}}^{\boldsymbol{0}} = K_\infty \boldsymbol{\Psi}_{\boldsymbol{kk}}^{\boldsymbol{0},\boldsymbol{ve}} \boldsymbol{\delta}_{\boldsymbol{ij}} + 2G_\infty \mathbb{e}_{\boldsymbol{ij}}^{\boldsymbol{0},\boldsymbol{ve}} + \sum_{m=1}^{M} \left[K_m \left(\boldsymbol{\Psi}_{\boldsymbol{kk}}^{\boldsymbol{0},\boldsymbol{ve}} \right) \boldsymbol{\delta}_{\boldsymbol{ij}} + 2G_m \left(\mathbb{e}_{\boldsymbol{ij}}^{\boldsymbol{0},\boldsymbol{ve}} \right) \right] \tag{21}$$

Summary of The Initial-Boundary Value Problems

Including the constitutive relations in **Equations 11** and **12**, **Table 1** summaries the IBVP for a linear viscoelastic solid. Here, $\boldsymbol{b_i}$ is the body force; $\boldsymbol{\sigma}_{\boldsymbol{ij}}^{\varsigma}$ and $\boldsymbol{e}_{\boldsymbol{ij}}^{\varsigma}$ are the components of stress and strain tensors, respectively; $\boldsymbol{u}_{\boldsymbol{i}}^{\varsigma}$ is the components of displacement vector; $\widetilde{\boldsymbol{u}}_{\boldsymbol{i}}$ is the initial displacement; $\overline{\boldsymbol{u}}_{\boldsymbol{i}}$ and $\boldsymbol{f_i}$ are the prescribed displacement and traction, respectively; $\boldsymbol{n_i}$ is the normal vector component on the boundary; T is the observation time in the natural time scale; τ_0 is the load period in the fast time scale; Ω denotes the spatial domain while Γ_u and Γ_f are the corresponding boundary portions where displacements $\overline{\boldsymbol{u}}_{\boldsymbol{i}}$ and tractions $\boldsymbol{f_i}$ are prescribed.

Table 1. The initial-boundary value problem for a linear viscoelastic solid.

Principle	Formulation
Equilibrium equation	$\boldsymbol{\sigma_{ij,j}} + \boldsymbol{b_i}(\vec{\boldsymbol{x}}, t, \tau)=0$ on $\Omega \times (0,T) \times (0,\tau_0)$
Constitutive equation	**Equations 11** and **12**
Kinematic equation	$\boldsymbol{e}_{\boldsymbol{ij}}^{\varsigma} = \left(\boldsymbol{u}_{\boldsymbol{i},\boldsymbol{j}}^{\varsigma} + \boldsymbol{u}_{\boldsymbol{j},\boldsymbol{i}}^{\varsigma} \right)/2$ on $\Omega \times (0,T) \times (0,\tau_0)$
Initial condition	$\boldsymbol{u}_{\boldsymbol{i}}^{\varsigma}(\vec{\boldsymbol{x}}, t = \tau = 0) = \widetilde{\boldsymbol{u}}_{\boldsymbol{i}}(\vec{\boldsymbol{x}})$ on Ω
Boundary condition	$\boldsymbol{u}_{\boldsymbol{i}}^{\varsigma} = \overline{\boldsymbol{u}}_{\boldsymbol{i}}(\vec{\boldsymbol{x}}, t, \tau)$ on $\Gamma_u \times (0,T) \times (0,\tau_0)$ $\boldsymbol{\sigma}_{\boldsymbol{ij}}^{\varsigma} \boldsymbol{n_j} = \boldsymbol{f_i}(\vec{\boldsymbol{x}}, t, \tau)$ on $\Gamma_f \times (0,T) \times (0,\tau_0)$

The IBVP in **Table 1** can be divided into the global and local IBVPs in the slow time scale and fast time scale, as shown in **Tables 2** and **3**. Each constitutive relation is obtained from the previous section. The transformation of the equilibrium equation, kinematic equation, initial condition, and boundary condition to the global and local parts can be found in the literature (Yu and Fish 2002a).

Table 2. The global initial-boundary value problem for a linear viscoelastic solid in the slow time scale.

Principle	Formulation
Equilibrium equation	$\langle \boldsymbol{\sigma}_{ij}^{\mathbf{0}} \rangle_{,j} + \langle \bar{\boldsymbol{b}}_i \rangle (\vec{\boldsymbol{x}}, t) = 0$ on $\Omega \times (0, T)$
Constitutive equation	**Equations 19** and **20**
Kinematic equation	$\langle \boldsymbol{e}_{ij}^{\mathbf{0}} \rangle = \left(\langle \boldsymbol{u}_{i,j}^{\mathbf{0}} \rangle + \langle \boldsymbol{u}_{j,i}^{\mathbf{0}} \rangle \right)/2$ on $\Omega \times (0, T)$
Initial condition	$\langle \boldsymbol{u}_i^{\mathbf{0}} \rangle (\vec{\boldsymbol{x}}, t = 0) = \tilde{\boldsymbol{u}}_i(\vec{\boldsymbol{x}})$ on Ω
Boundary condition	$\langle \boldsymbol{u}_i^{\mathbf{0}} \rangle = \langle \bar{\boldsymbol{u}}_i \rangle (\vec{\boldsymbol{x}}, t)$ on $\Gamma_u \times (0, T)$ $\langle \boldsymbol{\sigma}_{ij}^{\mathbf{0}} \rangle \boldsymbol{n}_j = \langle \boldsymbol{f}_i \rangle (\vec{\boldsymbol{x}}, t)$ on $\Gamma_f \times (0, T)$

Table 3. The local initial-boundary value problem for a linear viscoelastic solid in the fast time scale.

Principle	Formulation
Equilibrium equation	$\boldsymbol{\Phi}_{ij,j}^{\mathbf{0}} + \bar{\boldsymbol{b}}_i - \langle \bar{\boldsymbol{b}}_i \rangle = 0$ on $\Omega \times (0, \tau_0)$
Constitutive equation	**Equation 21**
Kinematic equation	$\boldsymbol{\Psi}_{ij}^{\mathbf{0}} = \left(\boldsymbol{\chi}_{i,j}^{\mathbf{0}} + \boldsymbol{\chi}_{j,i}^{\mathbf{0}} \right)/2$ on $\Omega \times (0, \tau_0)$
Initial condition	$\boldsymbol{\chi}_i^{\mathbf{0}} (\vec{\boldsymbol{x}}, \tau = 0) = 0$ on Ω
Boundary condition	$\boldsymbol{\chi}_i^{\mathbf{0}} = \bar{\boldsymbol{u}}_i - \langle \bar{\boldsymbol{u}}_i \rangle$ on $\Gamma_u \times (0, \tau_0)$ $\boldsymbol{\Phi}_{ij}^{\mathbf{0}} \boldsymbol{n}_j = \boldsymbol{f}_i - \langle \boldsymbol{f}_i \rangle$ on $\Gamma_f \times (0, \tau_0)$

Based on **Equations 8** to **10**, the zero-order reference solutions of the given IVBP can be obtained by combining the solutions of the global part in the slow time scale and local part in the fast time scale, shown as follows:

$$\boldsymbol{\sigma}_{ij}^{\mathbf{0}}(\vec{\boldsymbol{x}}, t, \tau) = \langle \boldsymbol{\sigma}_{ij}^{\mathbf{0}} \rangle (\vec{\boldsymbol{x}}, t) + \boldsymbol{\Phi}_{ij}^{\mathbf{0}}(\vec{\boldsymbol{x}}, t, \tau) \tag{22}$$

$$\boldsymbol{\varepsilon}_{ij}^{\mathbf{0}}(\vec{\boldsymbol{x}}, t, \tau) = \langle \boldsymbol{\varepsilon}_{ij}^{\mathbf{0}} \rangle (\vec{\boldsymbol{x}}, t) + \boldsymbol{\Psi}_{ij}^{\mathbf{0}}(\vec{\boldsymbol{x}}, t, \tau) \tag{23}$$

$$\boldsymbol{u}_{i}^{\mathbf{0}}(\vec{\boldsymbol{x}}, t, \tau) = \langle \boldsymbol{u}_{i}^{\mathbf{0}} \rangle (\vec{\boldsymbol{x}}, t) + \boldsymbol{\chi}_{i}^{\mathbf{0}}(\vec{\boldsymbol{x}}, t, \tau) \tag{24}$$

Equations 11 and **12** are used as the material constitutive relation and a default time-dependent solver is used to obtain the reference solution/cycle-by-cycle simulation of the original IBVP in the natural time scale for comparing with the temporal homogenization solution in the next section. The absolute value of relative error (AER) and the computational gain between the reference and temporal homogenization solutions are used to evaluate the computational accuracy and efficiency of the proposed model, as shown in **Equations 25** and **26**.

$$AER = \left| \frac{\phi_{ref} - \phi_{TH}}{\phi_{ref}} \right| \tag{25}$$

where ϕ_{ref} and ϕ_{TH} are the responses obtained from the reference solution and temporal homogenization solution, respectively.

$$\text{Computational gain} = \frac{T_{ref}}{T_{TH}} \tag{26}$$

where T_{ref} and T_{TH} are the computation time for the reference solution and temporal homogenization solution, respectively.

Figure 2 shows the flowchart of the temporal homogenization-based mechanical response modeling of viscoelastic solids (asphalt concrete is taken as a verification example in this paper).

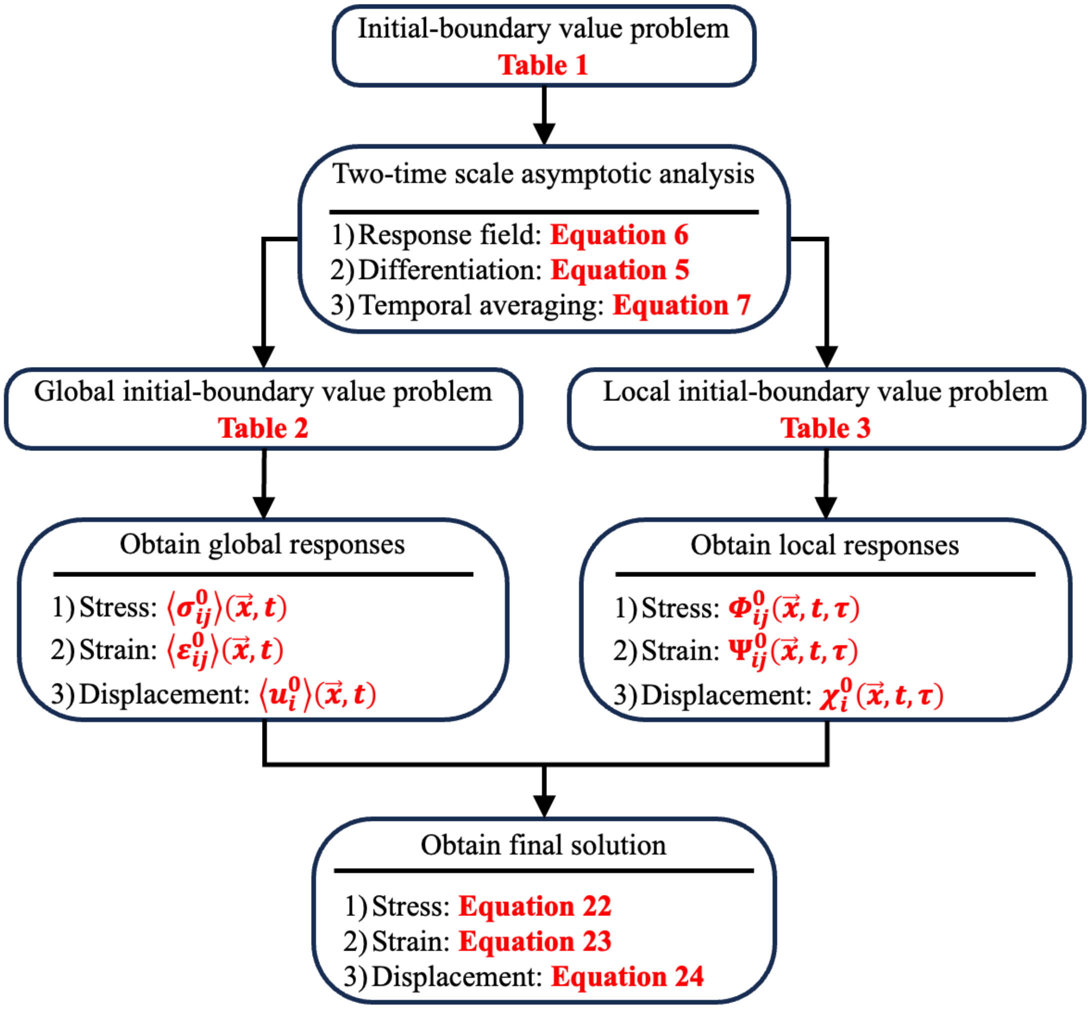

Figure 2. Flowchart for the temporal homogenization-based mechanical response modeling of viscoelastic solids.

VALIDATION EXAMPLES AND DISCUSSION

Uniaxial Cyclic Loading on A Cylindrical Sample of Asphalt Concrete

A stress-controlled uniaxial cyclic compression test with a haversine load waveform was performed on a cylindrical asphalt concrete sample. The used material properties and test results are from the authors' previous work (Zhang et al. 2015). A two-dimensional axisymmetric model has been established using

COMSOL Multiphysics® to conduct the FE modeling of the cylindrical sample to obtain the reference and temporal homogenization solutions. The axial strains obtained by the laboratory test and reference solution will be compared for validating the FE model. The responses obtained by the reference and temporal homogenization solutions will be compared to validate the accuracy and efficiency of the proposed temporal homogenization-based viscoelastic modeling of asphalt concretes. The material properties and testing conditions are detailed in **Table 4** and **Figure 3**.

Table 4. Viscoelastic properties of the cylindrical sample (Poisson's ratio: 0.32).

Component of relaxation modulus (MPa)		Component of relaxation time (s)	
E_∞	41.1	-	
E_1	3093.4	τ_1	1.0×10^{-6}
E_2	6040.0	τ_2	1.0×10^{-5}
E_3	6994.3	τ_3	1.0×10^{-4}
E_4	5565.7	τ_4	1.0×10^{-3}
E_5	3292.7	τ_5	1.0×10^{-2}
E_6	1649.0	τ_6	1.0×10^{-1}
E_7	525.1	τ_7	1.0×10^{0}
E_8	177.6	τ_8	1.0×10^{1}
E_9	129.7	τ_9	1.0×10^{2}
E_{10}	37.6	τ_{10}	1.0×10^{3}
E_{11}	2.9	τ_{11}	1.0×10^{4}

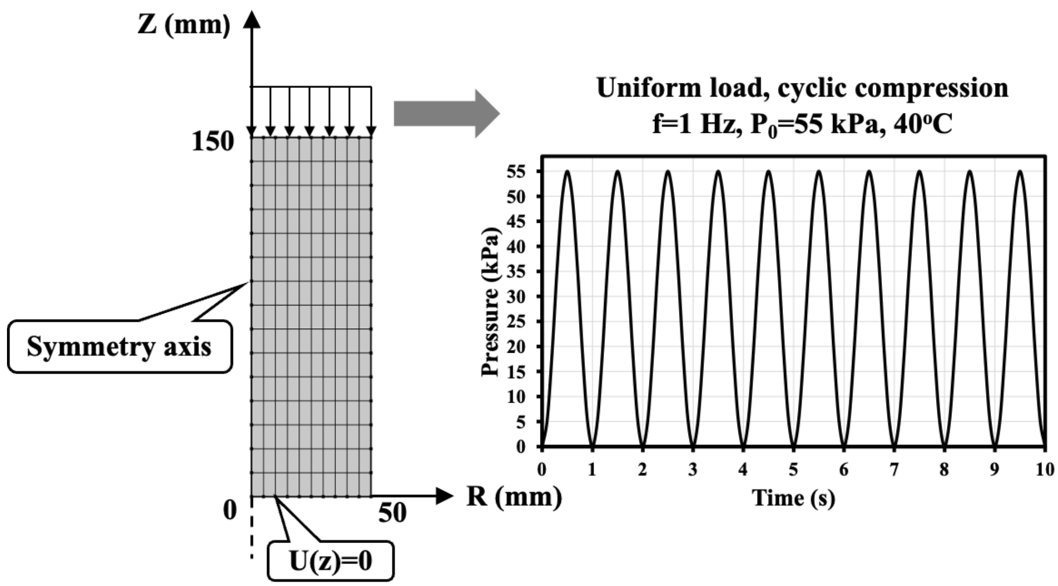

Figure 3. FE model of the cylindrical sample and the applied load.

Figure 4 compares the axial strains measured by laboratory tests and predicted by the reference solution of FE modeling. As can be seen, the evolutions of the measured and modeled axial strains are consistent, although the measured strain is greater (the maximum difference is around 30 με at the end of test) than the modeled one. The possible reasons are: (a) the loading amplitude of the cyclic load test is higher than the dynamic modulus test whose results were used to determine the linear viscoelastic parameters in **Table 4** (thus, the nonlinear response was not captured by the present linear material model); and (b) the viscoelastic model in this paper cannot capture the plastic deformation that may be induced to the sample. It can be concluded that the response fields of the cylindrical sample have not reached a steady state after 600 load cycles, which means more simulated load cycles are needed to capture a stable response in order to use the transfer functions in MEPDG.

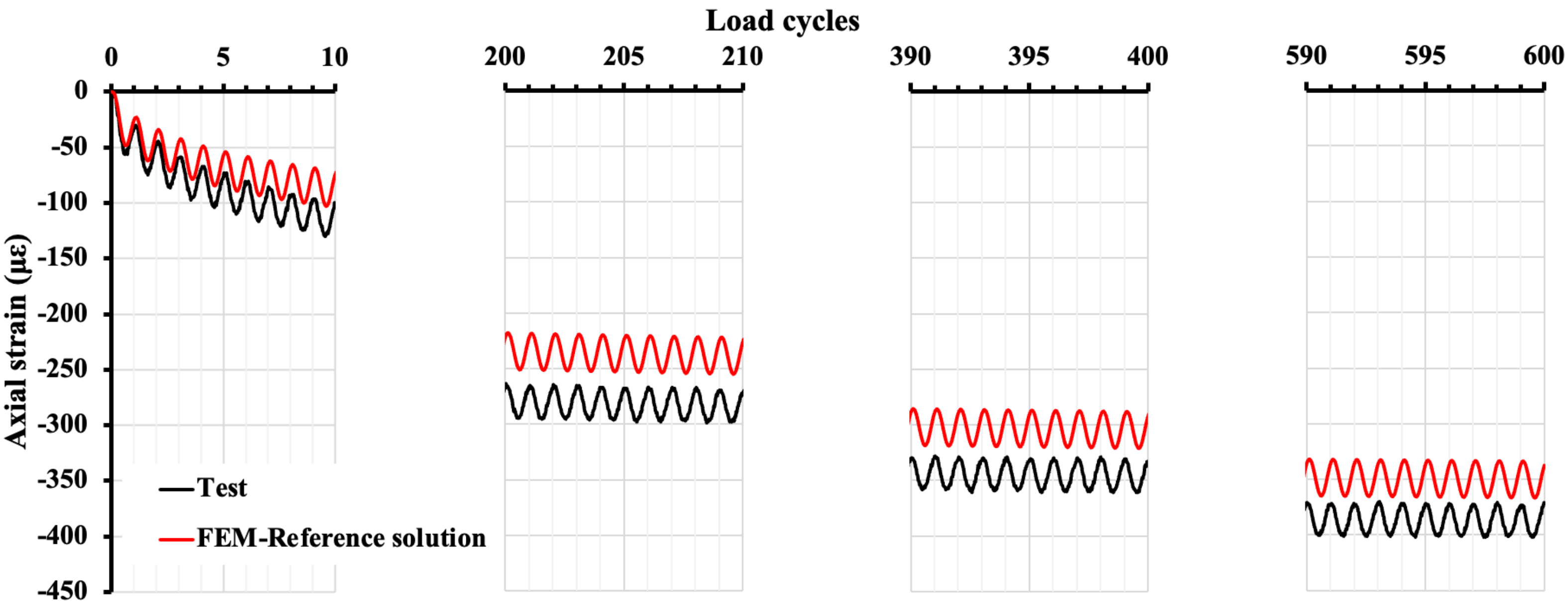

Figure 4. Comparison of the axial strains obtained by laboratory tests and reference solution of FE modeling.

Figures 5 and **6** demonstrate the comparisons of the reference solution and temporal homogenization solution for the IBVP via FE modeling. As can be seen, the temporal homogenization solution is consistent with the reference solution regarding on both of the long-term evolution and fast variation. **Figure 7** shows the computational accuracy and efficiency of the time homogenization-based modeling. As it is seen, the relative error decreases in absolute value with the number of load cycles. It is lower than 1% when the load cycles are more than 100 and relatively high difference only exists in the first a few cycles. Thus, the temporal homogenization-based viscoelastic response modeling demonstrates a sufficient accuracy when considering cyclic loading regarding the sample scale simulation. In addition, the computational time of the reference solution is 59 minutes while the computational time of temporal homogenization solution is about 4 minutes for modeling 10^4 load cycles, based on a workstation with an Intel® i9 CPU (@ 2.3 GHz). Besides, the computational gain increases with the number of cycles according to **Figure 7**. Thus, the computational gain of the temporal homogenization method is remarkable without the loss of evident simulation accuracy. The improvement of the computational efficiency comes from: (a) using a relatively large time increment to solve the global responses in the slow time scale; and (b) only one load cycle needs to be solved surrounding each slow time interval and the stress update is not necessary for the local responses in the fast time scale due to the periodic assumption (Lee and Shin 2023; Shin 2020; Yu and Fish 2002b).

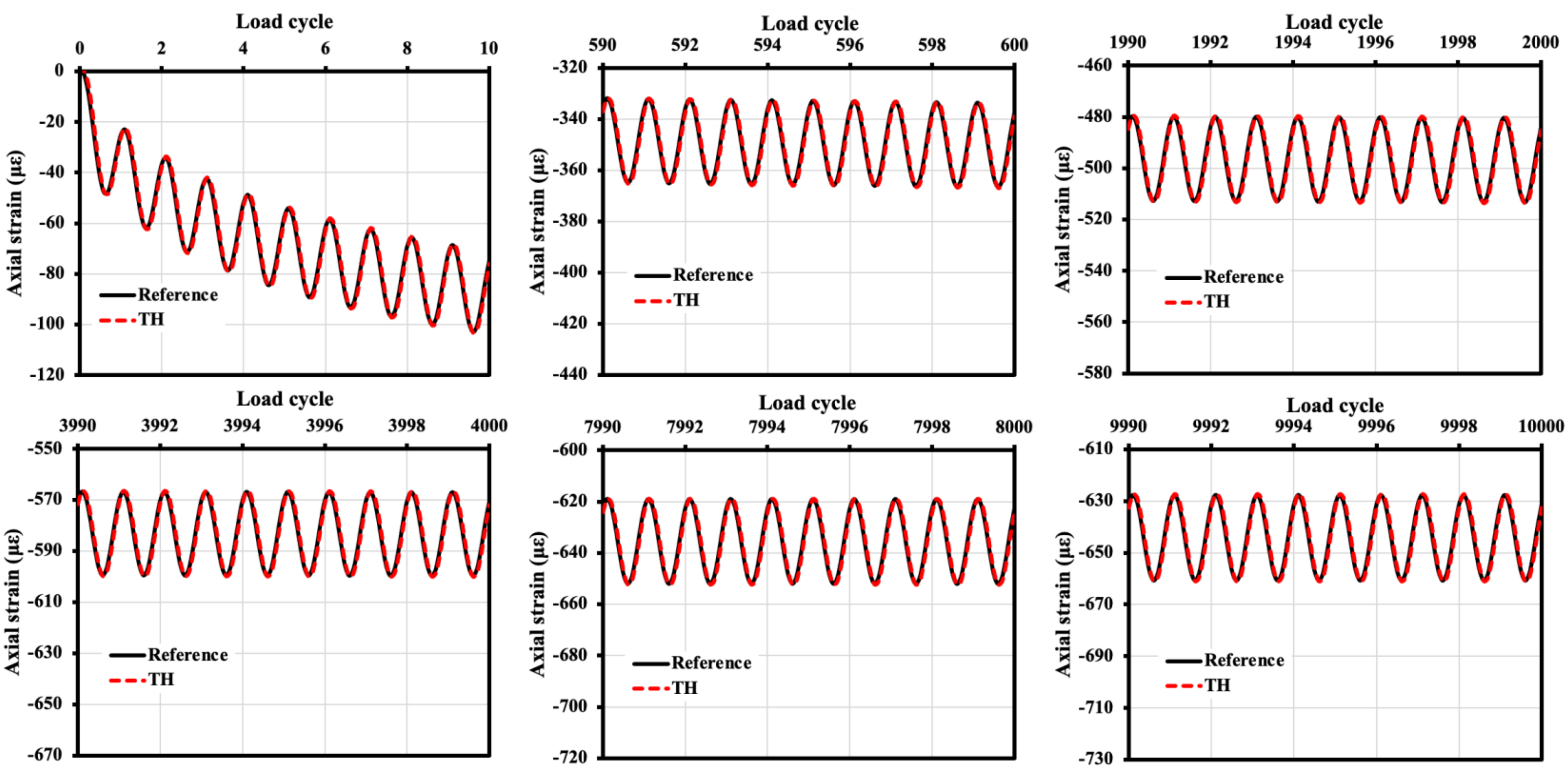

Figure 5. Comparison of the axial strains obtained by reference solution and temporal homogenization solution at different load cycles (TH refers to temporal homogenization).

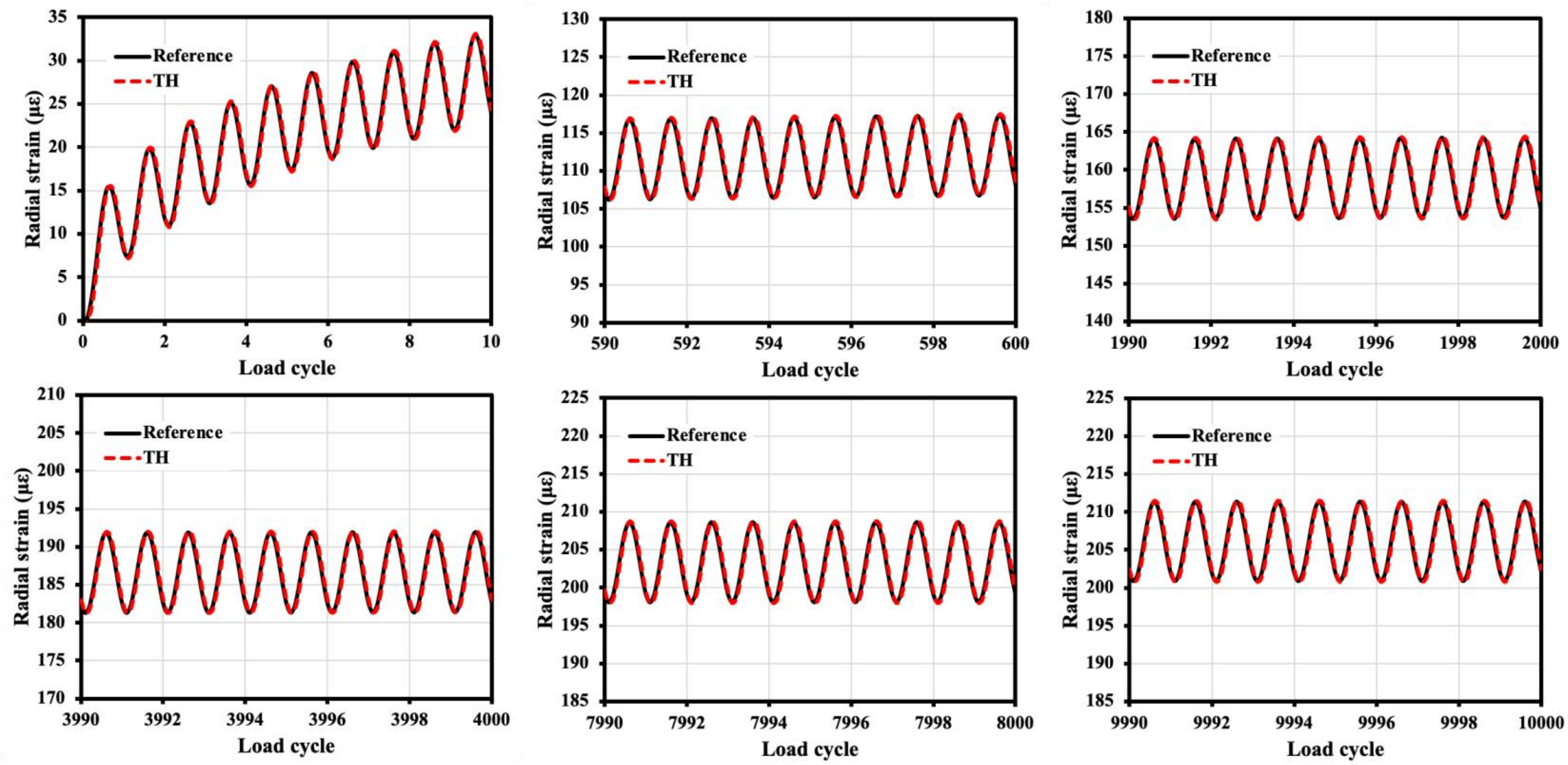

Figure 6. Comparison of the radial strains obtained by reference solution and temporal homogenization solution at different load cycles (TH refers to temporal homogenization).

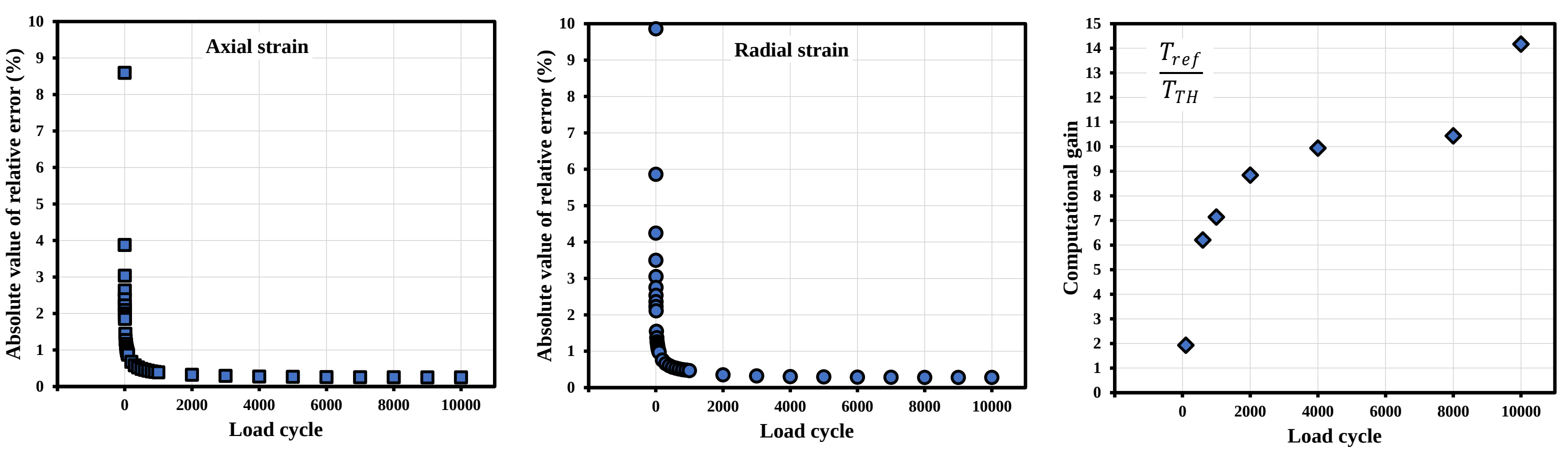

Figure 7. Accuracy and efficiency examination of the temporal homogenization modeling on the cylindrical asphalt concrete sample.

Locally Cyclic Loading on An Asphalt Pavement Structure

The mechanical responses of a typical semi-rigid base asphalt pavement structure are modeled using the reference and temporal homogenization methods. The pavement materials and structure are detailed in **Tables 5** and **6** and **Figure 8**, adopted from the authors' previous work (Luo et al. 2023). The three asphalt concrete layers are treated as the linear viscoelastic materials and the remaining layers are linear elastic materials. There are four transverse strain sensors embedded in the four corners of a rectangle area at the bottom of the lower asphalt layer, as shown in **Figure 8**. Two types of axle load (100 kN and 150 kN) were used to measure the pavement responses under normal and heavy vehicle load. The contact pressure of the two types of axle load were determined as 0.7 MPa and 0.91 MPa by the conversion relationship of **Equation 27** (Li and Huang 2004).

$$\frac{p_i}{p_0} = \left(\frac{P_i}{P_0}\right)^{0.65} \tag{27}$$

where p_i and P_i are the nonstandard contact pressure (MPa) and nonstandard axle load (kN), respectively; $p_0 = 0.7$ MPa is the standard contact pressure; and $P_0 = 100$ kN is the standard axle load.

Table 5. Material properties for each layer.

Material type	Layer	Density (kg/m^3)	Poisson's ratio	Modulus (MPa)
SMA-13, linear viscoelastic	Upper asphalt layer	2243	0.3	**Table 6**
SUP-20, linear viscoelastic	Middle asphalt layer	2243	0.3	**Table 6**
SUP-25, linear viscoelastic	Lower asphalt layer	2243	0.3	**Table 6**
Upper CBM, linear elastic	Upper base layer	2350	0.35	11500
Lower CBM, linear elastic	Lower base layer	2350	0.35	8500
Soil, linear elastic	Subgrade	2400	0.4	60

Note: SMA-13 refers to the stone mastic asphalt concrete with a 13 mm NMAS; SUP-20 refers to the Superpave asphalt concrete with a 20 mm NMAS; SUP-25 refers to the Superpave asphalt concrete with a 25 mm NMAS; CBM refers to the cement stabilized macadam; NMAS refers to the nominal maximum aggregate size.

Table 6. Viscoelastic properties of the three asphalt concretes.

	Component of relaxation modulus (MPa)			Component of relaxation time (s)	
	SMA-13	SUP-20	SUP-25		
E_∞	13.0	11.5	14.2	-	
E_1	1631.9	1637.8	2246.9	τ_1	1.0×10^{-6}
E_2	1102.2	2294.9	7272.1	τ_2	1.0×10^{-5}
E_3	3476.9	7649.7	8808.9	τ_3	1.0×10^{-4}
E_4	3659.7	5308.0	8027.5	τ_4	1.0×10^{-3}
E_5	2759.0	3092.8	5752.7	τ_5	1.0×10^{-2}
E_6	1188.9	1320.9	2433.9	τ_6	1.0×10^{-1}
E_7	579.6	579.5	921.7	τ_7	1.0×10^{0}
E_8	9.8	24.6	74.0	τ_8	1.0×10^{1}
E_9	32.7	31.2	125.4	τ_9	1.0×10^{2}
E_{10}	39.4	26.4	53.3	τ_{10}	1.0×10^{3}
E_{11}	55.7	32.4	150.4	τ_{11}	1.0×10^{4}

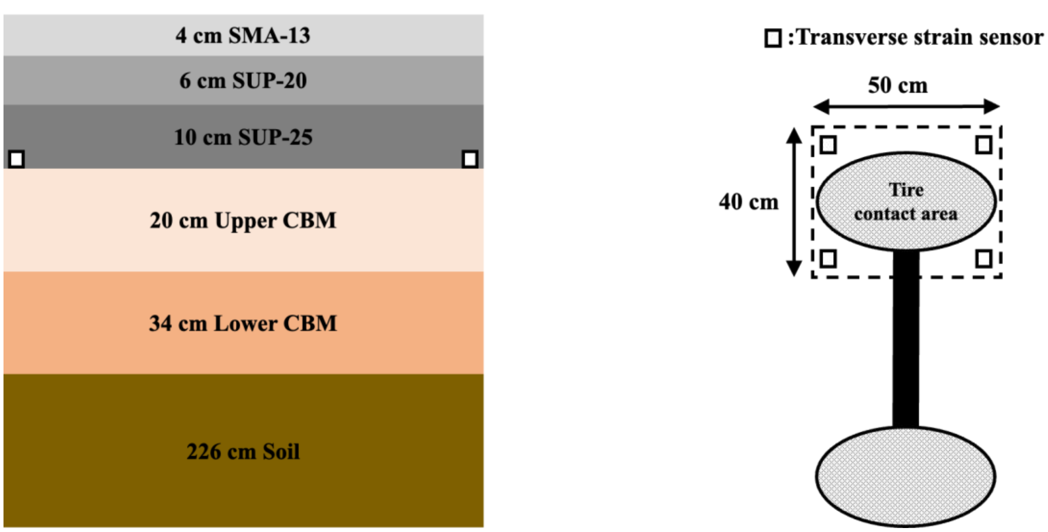

(a) (b)

(c)

(d)

Figure 8. Illustrations of pavement structure, strain sensor position, and field test: (a) pavement structure in vertical direction; (b) layout of the sensors and tire load; (c) embedded strain sensors; (d) creep-recovery field loading test.

Due to the limitations of monitoring resolution and sampling frequency of the strain sensors, the field loading scheme was designed as a static loading with a creep (7 min) and recovery (5 min) procedure. A three-dimensional pavement FE model was developed based on the exact structural and material information, as shown in **Figure 9-a.** All layers are assumed to be fully continuous. To validate the pavement FE model via the measured transverse strain, a creep and recovery scenario was simulated with the same field loading procedure, as shown in **Figure 9-c**. The contact area of the tire load was simplified as a square area with 0.3 m in length. **Figure 10** shows the comparison between the measured and modeled strain responses for the two contact pressures. The discrepancy at the high load level may be due to the presented viscoelastic model cannot capture the plastic deformation of asphalt concretes, so the residual strains at the end of recovery are almost the same under the two contact pressures. However, the modeled strains are overall consistent with the field measurements and the creep-recovery features can be well captured. Thus, the pavement FE model can be further used for comparing the accuracy and efficiency of the reference and time homogenization modeling subject to large numbers of cyclic loading.

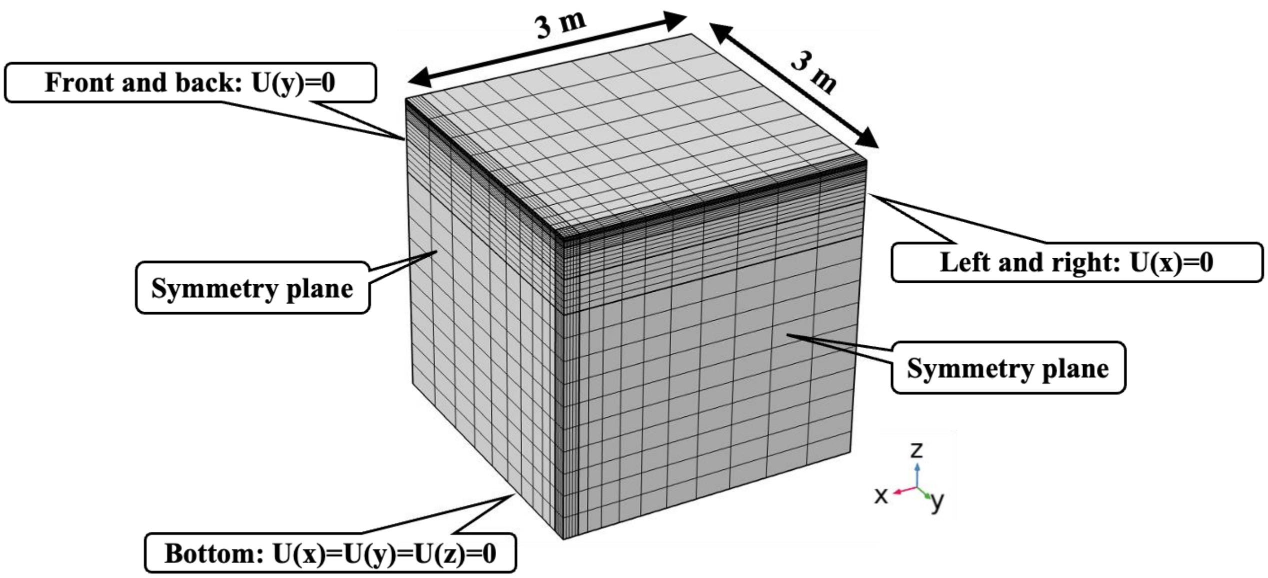
3 m
3 m
Front and back: U(y)=0
Left and right: U(x)=0
Symmetry plane
Symmetry plane
Bottom: U(x)=U(y)=U(z)=0
z
x
y

(a)

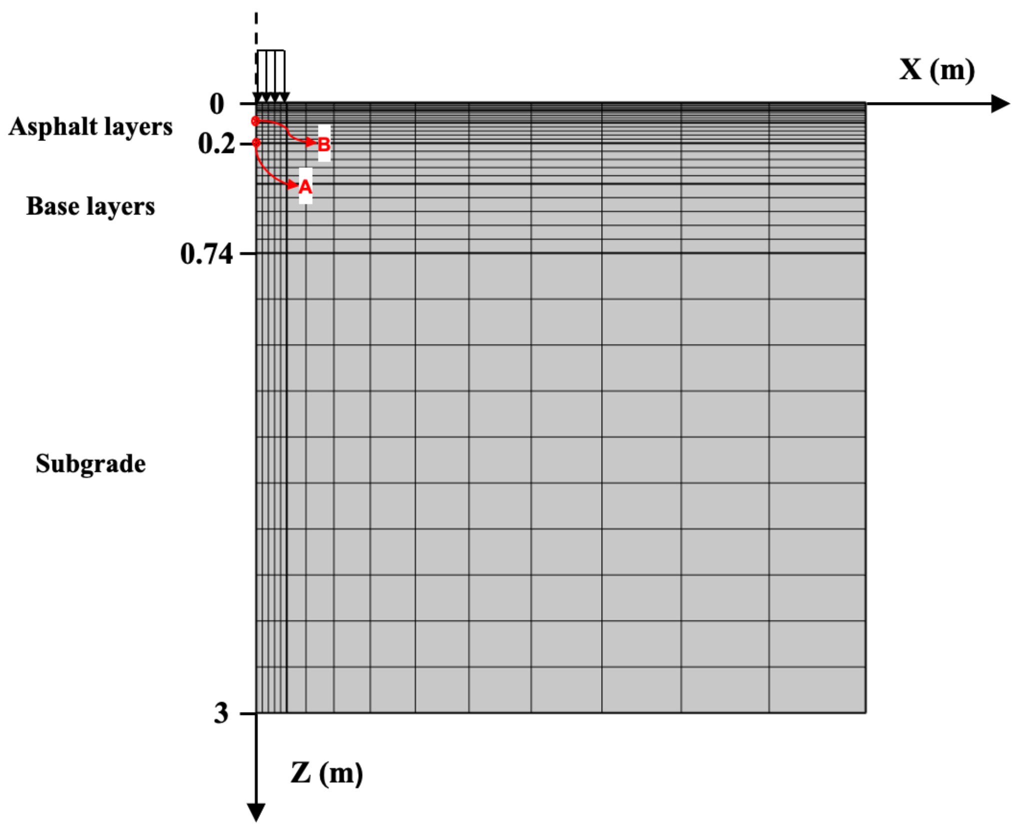
X (m)
0
Asphalt layers
0.2
B
A
Base layers
0.74
Subgrade
3
Z (m)

(b)

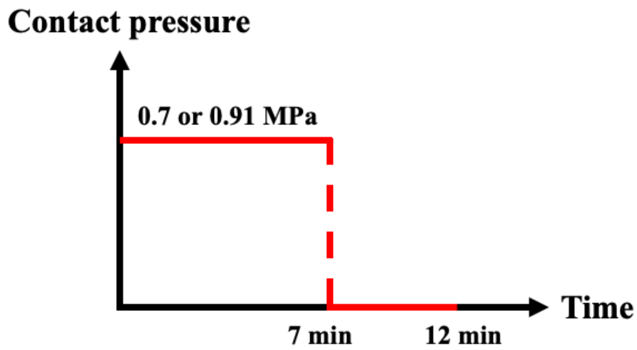

(c)

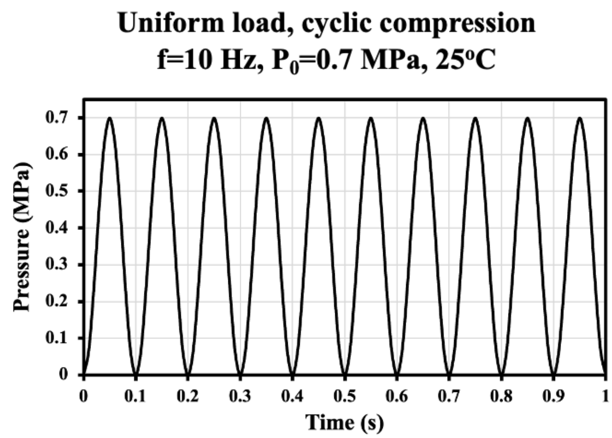

(d)

Figure 9. Illustrations of pavement FE model and loading schemes: (a) a quarter of FE model; (b) cross section of pavement structure; (c) loading scheme of the creep-recovery field test to validate the FE model; (d) cyclic loading to compare the reference and time homogenization solutions.

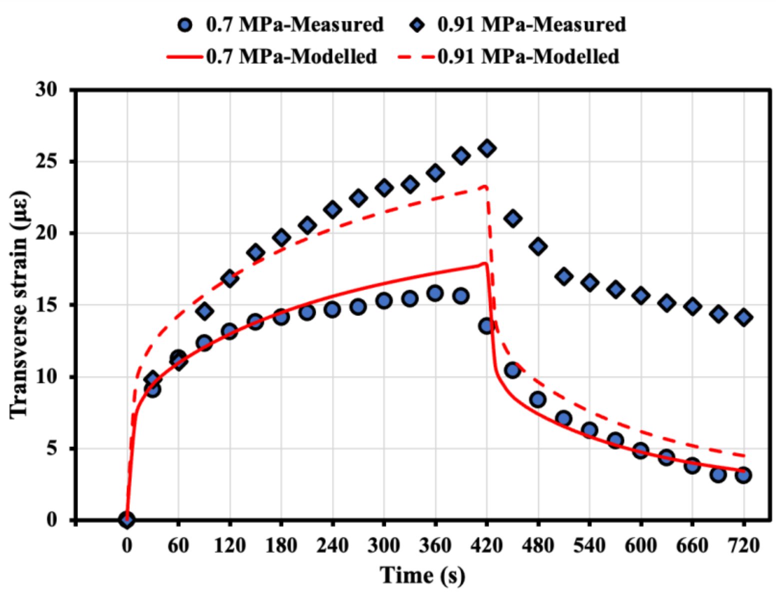

Figure 10. Comparison of the transverse strains obtained by field measurements and FE modeling for the creep-recovery loadings subject to two types of contact pressure.

In order to compare the reference and time homogenization solutions for a pavement structure under locally cyclic loading (**Figure 9-d**), two critical positions (**points A** and **B** in **Figure 9-b**) are selected to present their mechanical responses. Point A is at the bottom of the asphalt layer on the central line of the loading area and point B is at the middle of the asphalt layer on the central line of the loading area. Based on the current pavement design guide, the transverse strain of point A and vertical stress of point B are presented as the critical responses for the distress prediction models of asphalt pavements.

The results indicate that the temporal homogenization solution agrees well with the reference solution, as shown in **Figures 11** and **12**. The absolute value of relative error for the transverse strain of point A and vertical stress of point B are below 1% and 4% after 100 load cycles, which can be found in **Figure 13**. The computational time is reduced from 7 hours of the reference solution to around 38 minutes of the temporal homogenization solution for 10^3 load cycle simulation. An extrapolation regarding the computational gain versus the number of load cycles has been made in **Figure 13**. Assuming the annual average daily traffic (AADT) is 10^3, the temporal homogenization-based modeling approach can be approximately 10^3 times quicker than the reference solution to simulate the pavement responses after 27 years use (10^7 load cycles). Thus, it seems possible now to model the pavement responses and predict its long-term performance via the temporal homogenization method with an acceptable computing time.

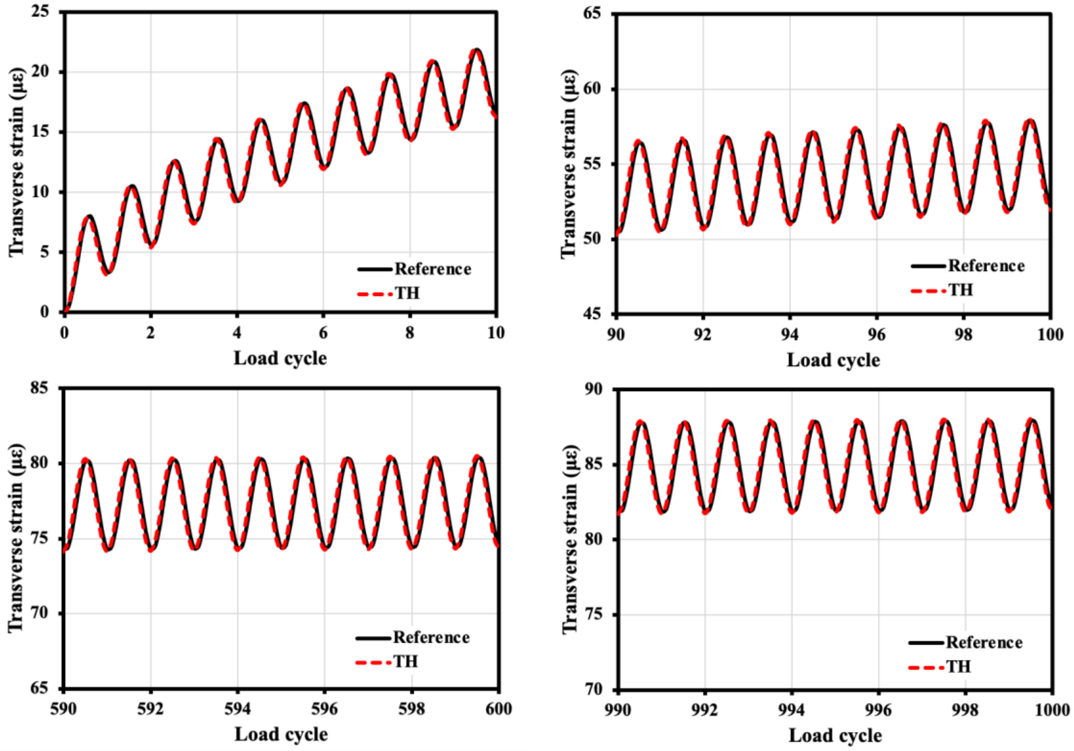

Figure 11. Comparison of the transverse strains (x-direction normal strain) of point A obtained by reference solution and temporal homogenization solution at different load cycles (TH refers to temporal homogenization).

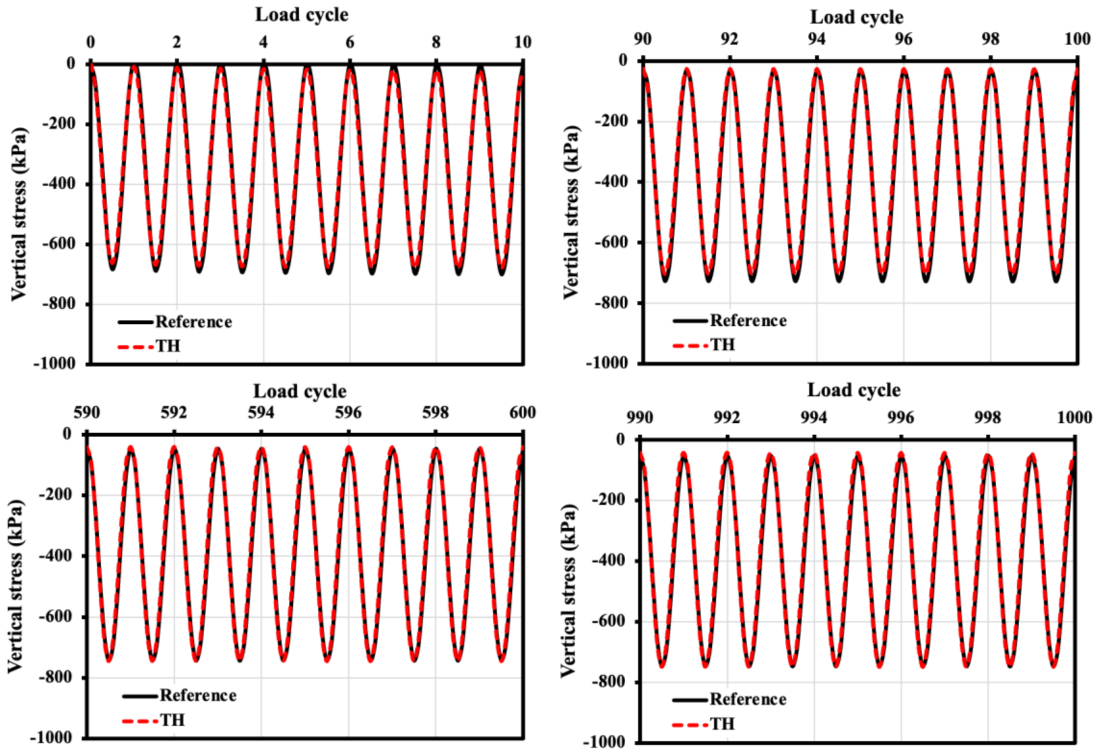

Figure 12. Comparison of the vertical stresses (z-direction normal stress) of point B obtained by reference solution and temporal homogenization solution at different load cycles (TH refers to temporal homogenization).

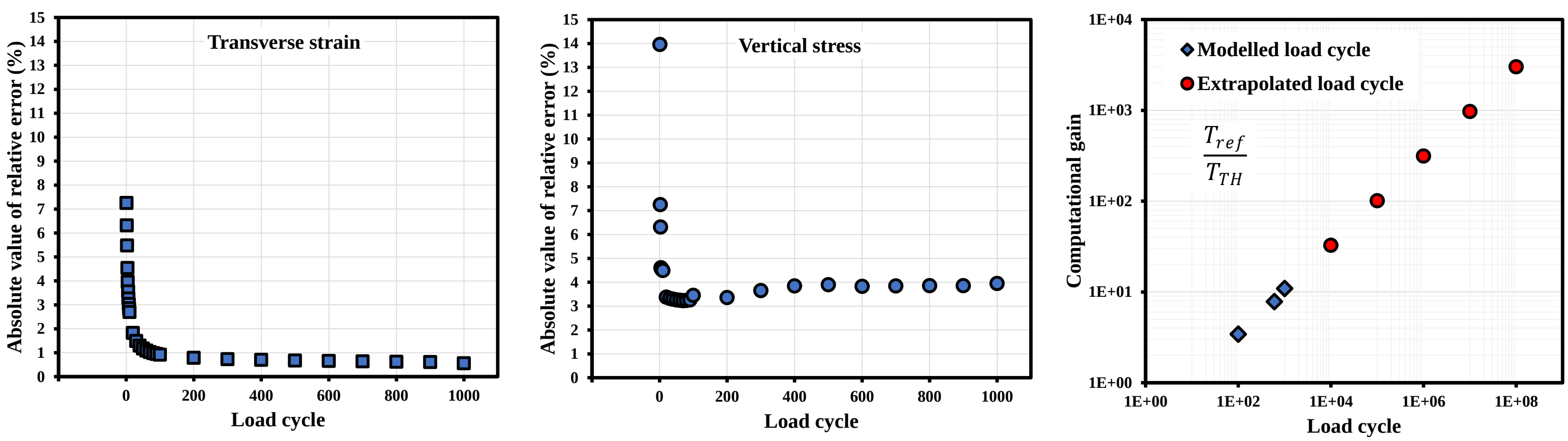

Figure 13. Accuracy and efficiency examination of the temporal homogenization modeling on the asphalt pavement structure.

CONCLUSIONS

This study introduces a highly efficient computational model to compute the viscoelastic responses of asphalt concretes and pavement structures under large numbers of cyclic loading. Multiple time scales were applied to an explicit constitutive relation of asphalt concretes to obtain the formula of global and local IBVPs. The temporal homogenization-based solutions were compared with the testing results and reference solutions for a cylindrical sample and a pavement structure to validate its computational accuracy and efficiency. The major conclusions are as follows:

- An explicit constitutive relation for viscoelastic solids in multiple time scales is developed based on the temporal homogenization.
- The temporal homogenization-based viscoelastic model saves considerable computational cost and maintains a satisfactory accuracy compared to the reference solution.
- The absolute values of relative error of the modeled responses between the time homogenization and reference solutions are lower than 1% and 4% for the cylindrical asphalt concrete and pavement structure under locally cyclic loadings, respectively.
- By using the proposed computational approach, only 4 minutes are needed to model the responses of a cylindrical asphalt concrete subject to 10^4 repeated load cycles under a uniaxial compression load.
- The computational time is reduced from 7 hours of the reference solution to 38 minutes of the temporal homogenization solution to model 10^3 load cycles of a pavement structure.

Future work will focus on predicting the pavement fatigue failure under cyclic loading by expanding the present temporal homogenization-based viscoelastic model to a viscoelastic-damage model.

DATA AVAILABILITY STATEMENT

Some or all data, models, or code that support the findings of this study are available from the corresponding author upon reasonable request.

- Axial strain of the uniaxial cyclic compression test on the cylindrical asphalt concrete.
- Transverse strain of the creep-recovery test on the field pavement section.

ACKNOWLEDGMENTS

The authors would like to acknowledge the financial support of a PhD studentship provided by the University of Nottingham, Nynas, and Colas. This work is also supported by the Asphalt Institute Foundation (AIF). This paper is supported by the Engineering and Physical Sciences Research Council (EPSRC) under Grant number: EP/W000369/1.

REFERENCES

AASHTO. 2020. *Mechanistic-Empirical Pavement Design Guide: A Manual of Practice. American Association of State Highway and Transportation Officials, Washington, DC.*

Abdelfattah, H. F. H., H. Baaj, and H. J. Kadhim. 2021. "Calibration of MEPDG permanent deformation models using Hamburg Wheel Rut Tester and field data." *International Journal of Pavement Engineering*, 0 (0): 1–16. Taylor & Francis. https://doi.org/10.1080/10298436.2021.1937622.

Behnke, R., and M. Kaliske. 2018. "Square block foundation resting on an unbounded soil layer: Long-term prediction of vertical displacement using a time homogenization technique for dynamic loading." *Soil Dynamics and Earthquake Engineering*, 115: 448–471. Elsevier Ltd. https://doi.org/10.1016/j.soildyn.2018.07.045.

Behnke, R., I. Wollny, F. Hartung, and M. Kaliske. 2019. "Thermo-mechanical finite element prediction of the structural long-term response of asphalt pavements subjected to periodic traffic load: Tire-pavement interaction and rutting." *Comput Struct*, 218: 9–31. Elsevier Ltd. https://doi.org/10.1016/j.compstruc.2019.04.003.

Bensoussan, A., J.-L. Lions, and G. Papanicolaou. 1978. *Asymptotic Analysis for Periodic Structures*. North-Holland Publishing Company.

Bhattacharyya, M., D. Dureisseix, and B. Faverjon. 2020. “A unified approach based on temporal homogenisation and cycle jump for thermo-mechanical combined cycle fatigue.” *Int J Fatigue*, 131. Elsevier Ltd. https://doi.org/10.1016/j.ijfatigue.2019.105320.

Chen, F., R. Balieu, and N. Kringos. 2017. “Thermodynamics-based finite strain viscoelastic-viscoplastic model coupled with damage for asphalt material.” *Int J Solids Struct*, 129: 61–73. Elsevier Ltd. https://doi.org/10.1016/j.ijsolstr.2017.09.014.

Cognard, J.-Y., and P. Ladevèze. 1993. “A large time increment approach for cyclic viscoplasticity.” *Int J Plast*, 9: 141–157. https://doi.org/10.1016/0749-6419(93)90026-M.

Cojocaru, D., and A. M. Karlsson. 2006. “A simple numerical method of cycle jumps for cyclically loaded structures.” *Int J Fatigue*, 28 (12): 1677–1689. https://doi.org/10.1016/j.ijfatigue.2006.01.010.

Devulder, A., D. Aubry, and G. Puel. 2010. “Two-time scale fatigue modelling: Application to damage.” *Comput Mech*, 45 (6): 637–646. Springer Verlag. https://doi.org/10.1007/s00466-010-0476-2.

Eslaminia, M., and M. N. Guddati. 2016. “Fourier-finite element analysis of pavements under moving vehicular loading.” *International Journal of Pavement Engineering*, 17 (7): 602–614. Taylor and Francis Ltd. https://doi.org/10.1080/10298436.2015.1007237.

Eslaminia, M., S. Thirunavukkarasu, M. N. Guddati, and Y. R. Kim. 2012. “Accelerated Pavement Performance Modeling Using Layered Viscoelastic Analysis.” 497–506.

Guennouni, T. 1988. “Sur une méthode de calcul de structuressoumises à des chargements cycliques :l’homogénéisation en temps.” *Mathematical Modelling and Numerical Analysis*, 22.

Haouala, S., and I. Doghri. 2015. “Modeling and algorithms for two-scale time homogenization of viscoelastic-viscoplastic solids under large numbers of cycles.” *Int J Plast*, 70: 98–125. Elsevier Ltd. https://doi.org/10.1016/j.ijplas.2015.03.005.

Kim, R. 2009. *Modeling of Asphalt Concrete*. *Modeling of Asphalt Concrete*, (Y. Richard Kim, ed.). McGraw-Hill.

Kim, S., H. Ceylan, and K. Gopalakrishnan. 2007. “Effect of M-E design guide inputs on flexible pavement performance predictions.” *Road Materials and Pavement Design*, 8 (3): 375–397. https://doi.org/10.3166/rmpd.8.375-397.

Lee, W., and H. Shin. 2023. “Temporal homogenization formula for viscoelastic–viscoplastic model subjected to local cyclic loading.” *Int J Numer Methods Eng*, 124 (4): 808–833. John Wiley and Sons Ltd. https://doi.org/10.1002/nme.7143.

Lemaitre, J., and Rodrigue. Desmorat. 2005. *Engineering damage mechanics : ductile, creep, fatigue and brittle failures*. Springer.

Li, H., and X. Huang. 2004. “Axle load conversion formula based on deflection equivalent for semi-rigid base asphalt pavement under heavy-load.” *Journal of Highway and Transportation Research and Development*, 21 (7): 5–8.

Luo, X., H. Wang, S. Cao, J. Ling, S. Yang, and Y. Zhang. 2023. “A hybrid approach for fatigue life prediction of in-service asphalt pavement.” *Philosophical Transactions of the Royal Society A: Mathematical, Physical and Engineering Sciences*, 381 (2254). Royal Society Publishing. https://doi.org/10.1098/rsta.2022.0174.

Lytton, R. L., J. Uzan, E. G. Fernando, R. Roque, D. Hiltunen, and S. M. Stoffels. 1993. *Development and Validation of Performance Prediction Models and Specifications for Asphalt Binders and Paving Mixes*. *Shrp-a-357*.

Shen, K., H. Wang, H. Zhang, J. Tong, and X. Chen. 2022. “SAPAVE: an improved semi-analytical FE program for dynamic viscoelastic analysis of asphalt pavement.” *International Journal of Pavement Engineering*, 23 (9): 3024–3035. Taylor and Francis Ltd. https://doi.org/10.1080/10298436.2021.1878516.

Shin, H. 2020. “Temporal homogenization formulation on general linear viscoelastic materials subjected to locally periodic loading.” *Int J Solids Struct*, 196–197: 1–9. Elsevier Ltd. https://doi.org/10.1016/j.ijsolstr.2020.03.026.

Tarefder, R., and J. I. Rodriguez-Ruiz. 2013. “Local calibration of MEPDG for flexible pavements in New Mexico.” *J Transp Eng*, 139 (10): 981–991. https://doi.org/10.1061/(ASCE)TE.1943-5436.0000576.

Yu, Q., and J. Fish. 2002a. “Temporal homogenization of viscoelastic and viscoplastic solids subjected to locally periodic loading.” *Comput Mech*, 29 (3): 199–211. Springer Verlag. https://doi.org/10.1007/s00466-002-0334-y.

Yu, Q., and J. Fish. 2002b. “Multiscale asymptotic homogenization for multiphysics problems with multiple spatial and temporal scales: a coupled thermo-viscoelastic example problem.” *Int J Solids Struct*. https://doi.org/10.1016/S0020-7683(02)00255-X.

Zhang, H., and Y. Zhang. 2023. “A time-temperature-ageing shift model for bitumen and asphalt mixtures based on free volume theory.” *International Journal of Pavement Engineering*, 24 (1). Taylor and Francis Ltd. https://doi.org/10.1080/10298436.2022.2138882.

Zhang, Y., B. Birgisson, and R. L. Lytton. 2015. “Weak Form Equation-Based Finite-Element Modeling of Viscoelastic Asphalt Mixtures.” *Journal of Materials in Civil Engineering*. https://doi.org/10.1061/(ASCE)MT.1943-5533.